



Studies on Nd-doped Barium Cerate Nano-Sized Catalyst in Converting CH₄ into CO₂ at Lower Temperature

Khalid Ouzaouit¹, Abdelhay Aboulaich^{2*}

¹IM2NP Institute (UMR CNRS 7334), Sud Toulon-Var University, BP.132, 83957 La Grade, France

²Materials Science and Nano-Engineering Department, Mohammed VI Polytechnic University (UM6P), Lot 660, Hay Moulay Rachid, 43150 Benguerir, Morocco

Received: 03.08.2021 Accepted: 30.08.2021 Published: 30-09-2021

*Abdelhay.ABOULAICH@um6p.ma

ABSTRACT

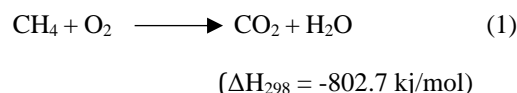
The present paper describes the synthesis and first application of Nd-doped Barium cerate (BaCeO₃) nanoparticles as catalyst for the catalytic oxidation of methane (CH₄) into CO₂. Nd-doped BaCeO₃ nanoparticles, with the formula BaNd_xCe_(1-x)O₃, have been prepared using a simple sol gel method starting from acetate precursors. The as-prepared nanoparticles have been fully characterized by XRD, TEM, HRTEM and specific surface area measurements. Results confirmed the formation of highly crystallized nano-sized particles with small crystallite size. In-situ FTIR spectroscopy was used to study the catalytic conversion of methane (CH₄) into CO₂ in the presence of the as-prepared Nd-doped BaCeO₃ nanocatalyst. The catalytic properties of such nanocatalysts have been discussed and correlated to Nd-doping rate, crystallite diameter and specific surface area of the materials. Excellent catalytic properties have been obtained with BaNd_{0.05}Ce_{0.95}O₃, such as superior conversion efficiency, longer catalysis lifetime and lower activation temperature compared to un-doped BaCeO₃ catalyst. Interestingly, it was found that BaNd_{0.05}Ce_{0.95}O₃ nanocatalyst successfully converts the totality of CH₄ present in a mixture of CH₄-Air into CO₂ at a much lower temperature compared to the conventional Pd/Al₂O₃ catalyst.

Keywords: Oxidation of CH₄; Nd-doped BaCeO₃, Nanocatalysts, Noble metal-free catalysts, Sol-gel method, Greenhouse Gases (GHG).

1. INTRODUCTION

The threat of climate change to our planet is today greater than it has ever been. Global warming is one of the most serious effects of climate change. In both 2019 and 2020, the World Economic Forum (WEF) identified global warming and the failure of climate change adaptation and mitigation as one of the highest and most probable global risks for humanity. Global warming is in particular due to the increasing levels of greenhouse gases (GHGs), including carbon dioxide (CO₂), methane (CH₄) and nitrous oxide (N₂O), released in the atmosphere (Matthews *et al.* 2008). Such GHGs, which can last for years to centuries in the atmosphere, trap heat by absorbing solar radiation and cause the planet to get hotter. This alarming situation led to a global mobilization to achieve a deep reduction of GHG emission, which needs strong support from the scientific community. The reduction of fossil-based energy production, CO₂ emission from industrial plants, CO₂ capture and storage have been proposed and developed as a solution to climate change (Rishee Kumar Singh *et al.* 2020; Friedlingstein *et al.* 2020). Surprisingly, the capture of methane or its oxidation has not received the same attention as air capture of CO₂, while CH₄ is about

25 times more effective than CO₂ at trapping infrared radiation and causing global warming (Boucher *et al.* 2010). CH₄ is also the second most important anthropogenic GHG. Its atmospheric concentration is about 5 billion tonnes (Gt) vs 40 Gt of CO₂ in 2018. Recent reports stated that the oxidation of the 5 Gt of CH₄ currently available in the atmosphere would yield 8.2 Gt additional atmospheric CO₂, equivalent to a few months of current industrial CO₂ emission, but it would remove about 1/6 of total radiative forcing (Jackson *et al.* 2019). The reduction in short-term warming, attributable to the high radiative forcing of CH₄, could thus offer a complementary strategy to the removal of long-lived GHGs such as CO₂ and N₂O. The oxidation of CH₄ to CO₂ is a thermodynamically favorable reaction as shown by reaction 1.



However, as the C-H bond is highly stable, high activation energy is needed to split the methane's C-H bond and that is why methane conversion is usually operated at high temperature (600⁻¹-1100 °C) (Cui *et al.* 2018). In order to overcome this high activation energy,

catalytic oxidation of methane is used. The reaction is generally catalyzed by supported or unsupported metal oxide catalysts, such as Co_3O_4 , $\text{Co}_3\text{O}_4/\text{Al}_2\text{O}_3$, ZnCrO_4 , CuCrO_4 , PbCrO_4 , $\text{Cr}_2\text{O}_3/\text{Al}_2\text{O}_3$, $\text{CuO}/\text{Al}_2\text{O}_3$ and $\text{CeO}_2/\text{Al}_2\text{O}_3$, and noble metals based-catalysts such as $\text{Pd}/\text{Al}_2\text{O}_3$, $\text{Pt}/\text{Al}_2\text{O}_3$, $\text{Rh}/\text{Al}_2\text{O}_3$, Pt/SiO_2 , Pd/SiO_2 , etc. (Lee *et al.* 1995). Among the metal oxide catalysts, Co_3O_4 catalyst provided the highest activity, but its activity was much lower than Pd/alumina catalysts (Lee *et al.* 1995). Photocatalytic oxidation of CH_4 , using ZnO , TiO_2 or metal-doped TiO_2 photocatalysts, has also been proposed in the literature (De_Richter *et al.* 2017). Perovskite-type oxide catalysts have also been studied for the catalytic oxidation of CH_4 (Arai *et al.* 1986). The highest active perovskite catalyst was $\text{La}_{0.6}\text{Sr}_{0.4}\text{MnO}_3$, which showed similar activity to $\text{Pt}/\text{Al}_2\text{O}_3$ catalyst at a conversion level below 80%. However, unlike the Pt/alumina catalyst, the catalytic activity with increasing temperature was significantly reduced at high conversion levels (Shimazaki *et al.* 2011). Even though, much progress has been made in decreasing the oxidation temperature of CH_4 , most of the catalysts mentioned above still need temperature higher than 300 – 500 °C so that the CH_4 oxidation reaction can occur. Hence, the replacement of noble metal in CH_4 oxidation catalysts, while keeping high CH_4 conversion efficiency and low reaction temperature, remains a big challenge.

BaCeO_3 -based ceramics and related compounds are very important materials because of their thermal and chemical stability and good ionic conduction properties, which allow these materials to be used in a wide range of applications, such as fuel cells, hydrogen separation membranes and hydrogen sensors (Yamanaka *et al.* 2003; Su *et al.* 2006; Bhowmick *et al.* 2010; Senthil Kumar *et al.* 2017; Madhuri Sailaja *et al.* 2017). Recently, some attempts have also been made to assess the catalytic properties of BaCeO_3 in the oxidative coupling of CH_4 and its conversion to C_2 products, like ethane and ethylene (Igenegbai *et al.* 2018).

In this study, the synthesis and the first application of Nd-doped BaCeO_3 nano-sized oxide in total conversion of CH_4 into CO_2 has been reported. The as-synthesized nanocatalyst showed very high conversion efficiency (up to 99.4 %) at much lower temperature compared to the conventional noble metal-based $\text{Pd}/\text{Al}_2\text{O}_3$ catalyst. The Nd doping rate of the as-prepared catalysts has been varied and correlated with nanocrystals diameter and specific surface area. The effect of all these parameters on the CH_4/CO_2 conversion efficiency in the presence of Nd-doped BaCeO_3 nanocatalysts has also been studied.

2. MATERIALS AND METHODS

2.1 Synthesis Method

In the first step, an appropriate amount of barium acetate (99.9 %), cerium acetate (99.9 %) and

neodymium acetate (99.9%), supplied from Aldrich, corresponding to the theoretical formula of $\text{BaNd}_x\text{Ce}_{(1-x)}\text{O}_3$, with x varied from 0 to 0.15, were dissolved in isopropanol. Then, the mixture was stirred for 1 hour until the total dissolution of the solid content in the solvent. The obtained solution was then heated at 80 °C under continuous stirring until formation of gel. The resulting gel was dried at 80 °C for 12 hours. Finally, the as-prepared powder was ground in an agate mortar and calcined at 950 °C for 5 hours with a heating and cooling rate of 5 °C/min. $\text{Pd}/\text{Al}_2\text{O}_3$ commercial catalyst containing 5% Pd (Sigma Aldrich) was used in this study for comparison.

2.2. Structural and Morphological Characterization

The XRD patterns were recorded using a Siemens – Brucker D5000 diffractometer. After a preliminary indexation using Winploter software, the lattice parameters were calculated and refined by least squares method (Roisnel *et al.* 2001). Crystallites sizes of the synthesized powders were estimated using Debye-Scherrer formula. Scanning electron microscopy (SEM) analyses were carried out using PHILIPS XL30 equipment in order to characterize the morphology of as-prepared catalysts. The thermal decomposition of the air-dried gel precursor of $\text{BaNd}_x\text{Ce}_{(1-x)}\text{O}_3$ catalyst was investigated using differential thermal analysis (DTA) and thermogravimetric analysis (TGA), which have been carried out in the temperature range of 25 – 1100 °C with a TG-DTA 92 SETARAM equipment, with a heating rate of 5 °C/min. In order to characterize the porosity of the synthesized materials, nitrogen sorption isotherms were recorded at 77.35 K using a MICROMERITICS ASAP 2020 automatic apparatus, after an outgassing process of 12 hours at 90 °C under secondary vacuum. The specific surface area was determined by the Brunauer–Emmett–Teller (BET) method (Brunauer *et al.* 1938).

2.3. Experimental set-up for catalytic test

The experimental set-up used to measure the catalytic activity of the $\text{BaNd}_x\text{Ce}_{(1-x)}\text{O}_3$ nanocatalysts, through the oxidation of CH_4 to CO_2 , is schematized in the Fig.1. It includes three parts:

- i) **Feed part** where the gas is supplied out using a bottle containing 2500 ppm of CH_4 diluted in air, one bottle containing pure oxygen (O_2) and the other one contains argon (Ar). The flowmeter is used to control the gas output. A mixer is used to prepare the gas mixture with desired composition. The catalytic oxidation of CH_4 was carried out with a fixed flow gas of 5 mL/minute.
- ii) **Reactor part** which includes a quartz tube held in place with silica wool on both sides. The quartz tube containing the catalyst powder was oriented

horizontally in a furnace and heated to the desired temperature at a rate of 2 K/min under argon flow.

iii) **Analysis part** or the analysis cell, where the outgoing gases are analyzed, is a quartz tube containing pellets

of KBr at its two ends. The cell is placed in a FTIR spectrophotometer. The FTIR spectra were recorded between 400 cm^{-1} and 4000 cm^{-1} , with a resolution of 8 cm^{-1} .

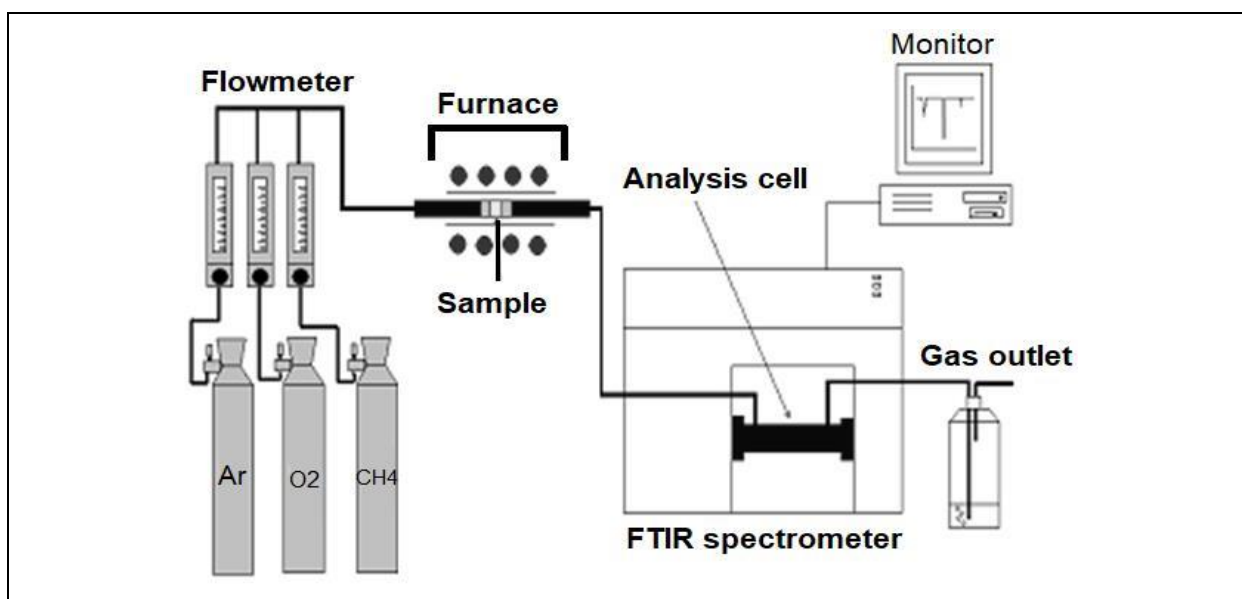


Fig. 1: The experimental set-up used in this study for the catalytic oxidation of CH_4 to CO_2

2.4. Catalytic activity measurement

In order to analyze the gas-solid reactivity over time and to evaluate the catalytic efficiency of our nanocatalysts at room and high temperature, in-situ FTIR measurements have been carried out according to the following procedure:

- First of all, the catalytic cell is heated at the desired temperature, without any catalyst, in order to perform the blank experiment and control the purity of the cell itself; argon gas is injected in the cell with a flow gas of 5 mL/minute and a series of FTIR spectra are recorded.
- Then, in order to define a new blank experiment with catalyst only (without any active gas), the catalyst sample is introduced in the quartz tube, then argon flux is injected to evacuate room atmosphere (air with residual CO_2 and H_2O gases), FTIR spectra are also recorded in these conditions.
- Finally, in order to perform the catalytic test, the active gas (air with 2500 ppm of methane CH_4) is introduced at the desired temperature and simultaneously, a sequence of FTIR spectra is recorded at about 1-minute intervals.

The catalytic reaction is then monitored by the evolution of FTIR bands of CH_4 (characteristic bands at 3020 cm^{-1} and 1300 cm^{-1}), CO_2 (characteristic bands at 2350 cm^{-1} and 670 cm^{-1}) and H_2O (characteristic band at 1590 cm^{-1}), as shown in Fig. 2 (Supplementary Material). Assuming that the FTIR band intensity is proportional to

the concentration of CH_4 and CO_2 , the concentration of CH_4 and CO_2 at time 't' can be calculated as below:

$$[\text{CH}_4]^* = I(\text{CH}_4)/I_{\text{max}}(\text{CH}_4)$$

with $I(\text{CH}_4)$ is the measured FTIR band surface of CH_4 and $I_{\text{max}}(\text{CH}_4)$ is the measured FTIR band surface of CH_4 in the absence of any catalytic interaction.

By the way, according to the reaction 1, when one mole of CH_4 is oxidized, one mole of CO_2 is formed. So, the concentration of CO_2 at time t can be calculated as below:

$$[\text{CO}_2]^* = 1 - [\text{CH}_4]^*$$

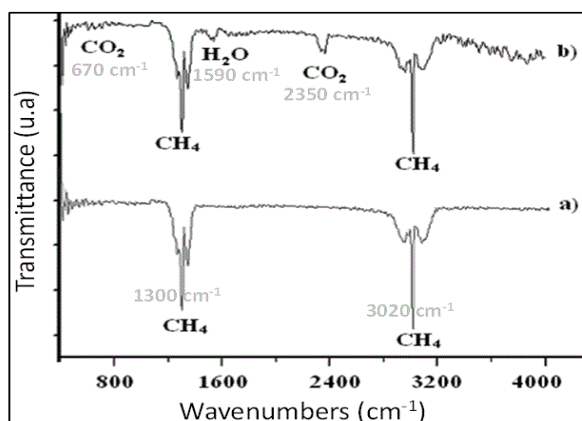


Fig. 2: Supplementary Material

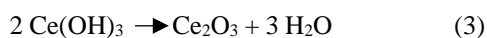
Relative normalized values $[\text{CH}_4]^*$ and $[\text{CO}_2]^*$ are then used to represent the conversion rate of CH_4 into CO_2 . For example, when $[\text{CO}_2]^*$ is equal to 1, this indicates a complete conversion of the 2500 ppm of CH_4 into 2500 ppm of CO_2 . The CO_2 band at 2350 cm^{-1} was finally chosen to follow the catalytic reaction, because of its better definition in the spectra (Fig. 2, Supplementary Material).

3. RESULTS AND DISCUSSION

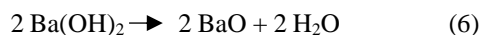
3.1 Preparation and characterization of nano-sized $\text{BaNd}_x\text{Ce}_{(1-x)}\text{O}_3$ catalysts

Fig. 3 (Supplementary Material) shows the TGA and TDA results of dried gel precursor corresponding to the un-doped BaCeO_3 catalyst. The curves show a multi-step decomposition behavior, with an endothermic peak at $130\text{ }^\circ\text{C}$, related to the loss of moisture and dehydration of the precursors, an exothermic peak at around $325\text{ }^\circ\text{C}$, which can be attributed to the decomposition of the organic content of the gel. However, no weight loss was observed at temperature higher than $950\text{ }^\circ\text{C}$. The reactions involved in the synthesis of BaCeO_3 can be written as below:

- For cerium precursor:



- For barium precursor:



Therefore, the formation of barium cerate occurs according to:

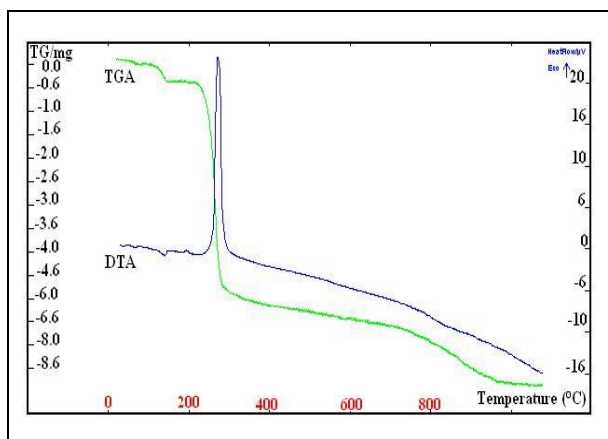


Fig. 3: Supplementary Material

The Fig. 4 shows the XRD pattern of $\text{BaNd}_x\text{Ce}_{(1-x)}\text{O}_3$ catalysts with different Nd content. The results showed that all the samples are well crystallized and all diffraction peaks of the samples are indexed as the orthorhombic perovskite structure, which matches with the JCPDS card number 22-0074.

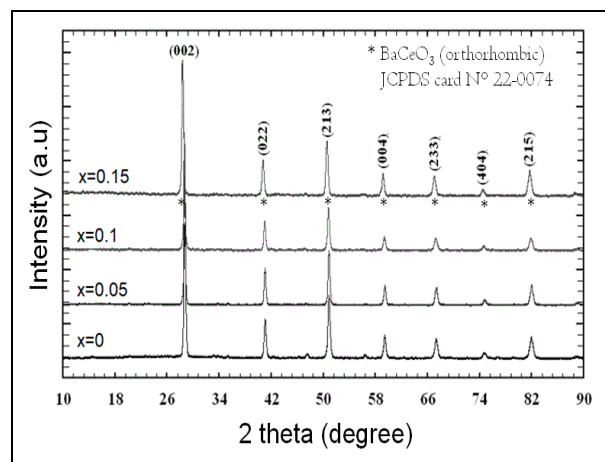


Fig. 4: XRD patterns of $\text{BaNd}_x\text{Ce}_{(1-x)}\text{O}_3$ catalysts with x variation from 0 to 0.15%

The lattice parameters and average crystallite size of the samples have been calculated from XRD patterns and results are summarized in Table 1. The calculated lattice parameters are in good agreement with the values reported in the literature (Senthil Kumar *et al.* 2017). Results also showed that no significant change is observed in the lattice parameters with increasing Nd doping, indicating a homogeneous dispersion of Nd in the BaCeO_3 structure where Ce^{4+} sites would be substituted with Nd^{3+} ions. This substitution is facilitated by the very similar ionic radii between Ce^{4+} (1.11 \AA) and Nd^{3+} (1.08 \AA).

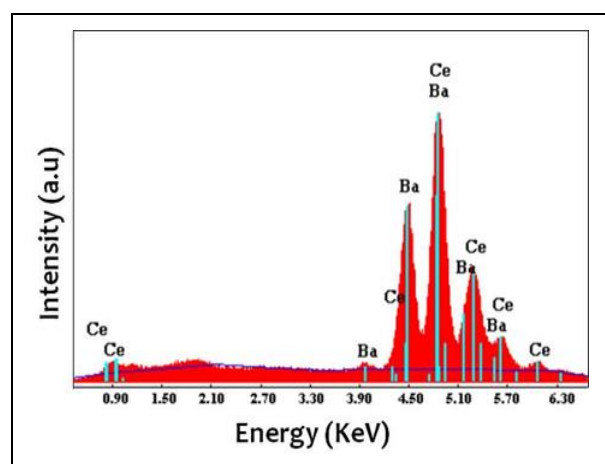
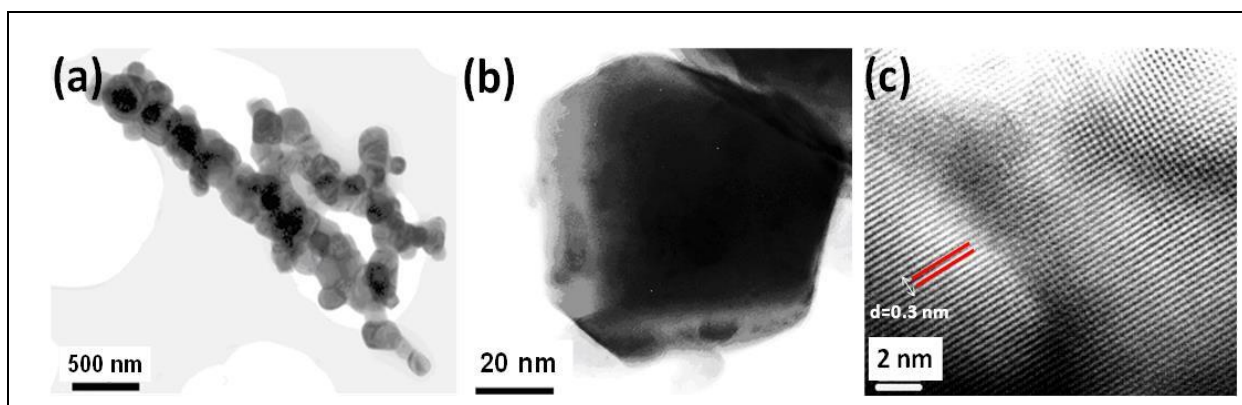


Fig. 5: Supplementary Material

Table 1: Lattice parameters and average crystallites size of $\text{BaNd}_x\text{Ce}_{(1-x)}\text{O}_3$ nanocatalysts

Catalyst	a (Å)	b (Å)	c (Å)	Average crystallite diameter (nm)
BaCeO_3	8.776 ± 0.002	6.212 ± 0.004	6.231 ± 0.002	19.6 ± 0.5
$\text{BaNd}_{0.05}\text{Ce}_{0.95}\text{O}_3$	8.775 ± 0.003	6.210 ± 0.004	6.228 ± 0.005	18.4 ± 0.5
$\text{BaNd}_{0.1}\text{Ce}_{0.9}\text{O}_3$	8.771 ± 0.002	6.211 ± 0.004	6.229 ± 0.004	17.3 ± 0.5
$\text{BaNd}_{0.15}\text{Ce}_{0.85}\text{O}_3$	8.772 ± 0.002	6.210 ± 0.003	6.228 ± 0.004	17.0 ± 0.5

**Fig. 6: TEM image (a) and HRTEM image (b-c) of $\text{BaNd}_{0.1}\text{Ce}_{0.9}\text{O}_3$ nanocatalyst**

Moreover, results showed that crystallite diameter significantly decreases from about 20 nm to 17 nm when x is increased from 0 to 0.15. In addition to XRD results, the chemical composition of un-doped BaCeO_3 catalyst was confirmed by EDS measurement (Fig. 5, Supplementary Material).

The as-prepared nanocatalysts have also been observed by TEM. We should note that all the samples have similar morphology, which consists of agglomerates of nanocrystals of about 100 nm as shown in Fig. 6(a), in the case of $\text{BaNd}_{0.1}\text{Ce}_{0.9}\text{O}_3$. The formation of agglomerate of particles could result from the high surface/volume ratio of the nanocrystals. By the way, since the crystallite diameter calculated from XRD showed smaller nanocrystals, the particle size measured from TEM image suggests that particles are polycrystalline. HRTEM image also shows that the particles are highly crystalline with a lattice fringe spacing of $d=0.3$ nm (image 3(c)), which corresponds to the (002) plane of BaCeO_3 perovskite structure. Table 2 provides the specific surface area of the as-prepared $\text{BaNd}_x\text{Ce}_{(1-x)}\text{O}_3$ catalysts calculated using BET method.

As can be seen from Table 2, all the samples exhibit a large surface area and thus are supposed to yield a high catalytic activity, since the heterogeneous catalytic reaction is generally enhanced by the high surface area of the catalyst. Results also showed that the surface area significantly increases with increasing Nd content, which

is in agreement with the decrease of crystallite diameter with increasing Nd content, already shown in Table 1.

Table 2: BET surface area of $\text{BaNd}_x\text{Ce}_{(1-x)}\text{O}_3$ nanocatalysts

Nanocatalyst	BET specific surface area (m^2g^{-1})
BaCeO_3	47.3
$\text{BaNd}_{0.05}\text{Ce}_{0.95}\text{O}_3$	53.7
$\text{BaNd}_{0.1}\text{Ce}_{0.9}\text{O}_3$	55.2
$\text{BaNd}_{0.15}\text{Ce}_{0.85}\text{O}_3$	56.5

3.2 Catalytic performance

3.2.1 Catalytic behavior of Nd-doped BaCeO_3 nanocatalysts

Fig. 7 shows the evolution of CH_4 conversion as a function of time at 300 °C in the presence of our $\text{BaNd}_x\text{Ce}_{(1-x)}\text{O}_3$ nanocatalysts. The obtained curves are similar and present three characteristic parts:

i) the first one, which corresponds to a rapid increase in CO_2 absorbance, indicating an increase in the conversion rate of CH_4 , can be associated with the active phase of the catalyst. This can be explained by the increasing adsorption of CH_4 on the active sites of the

catalyst due to constant flow rate of CH₄, flowing through the catalytic material, which is also enhanced by the high surface area of the nanocatalysts.

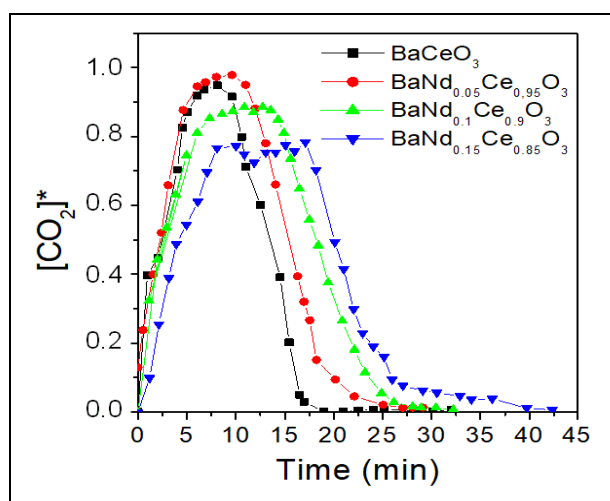


Fig. 7: Rate of catalytic conversion of CH₄ into CO₂ measured from FTIR spectroscopy (CO₂ vibrational band at 2350 cm⁻¹ was used for monitoring the catalytic reaction)

ii) the second part, which corresponds to the top part of the curves where a maximum CO₂ formation is reached, results from the saturation of surface-active sites of the catalysts; this is because adsorbed methane molecules have reacted and the corresponding active sites have lost their reactivity.

iii) the third phase, which corresponds to the decrease in CH₄ conversion rate, can be ascribed to the damping of the catalysts. This is because the surface-active sites of the catalyst are no longer available to gas molecules and the catalytic reaction is stopped.

The catalyst lifetime of our BaNd_xCe_(1-x)O₃ nanocatalysts, which is defined as the time difference between the beginning of CH₄ conversion and the end of the saturation phase, can be estimated from the [CO₂]* vs. time curves (Fig. 7). This time increases from 19 to 40 minutes when the Nd content (x) is increased from 0 to 0.15 %, respectively, as shown in Table 3.

Table 3: Catalyst lifetime and CH₄ conversion rate of BaNd_xCe_(1-x)O₃ nanocatalysts

Nd Content (x %)	CH ₄ conversion (%)	Catalyst lifetime (min)
0	95	19
0.05	98	25
0.1	88	28
0.15	78	40

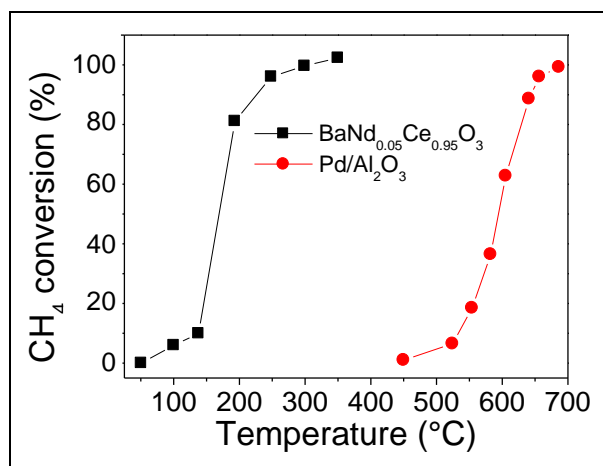


Fig. 8: The light-off curve of BaNd_{0.05}Ce_{0.95}O₃ nanocatalyst and Pd/Al₂O₃ commercial catalyst (CO₂ vibrational band at 2350 cm⁻¹ was used to calculate the conversion rate)

Interestingly, results show that the barium cerate nanocatalyst doped with 5% Nd (compared to Ce content), with the formula BaNd_{0.05}Ce_{0.95}O₃, yields higher CH₄ conversion rate and improved catalysis lifetime compared to un-doped BaCeO₃ catalyst. The result is also in agreement with the surface area measurements (Table 2), which showed higher specific surface area for BaNd_{0.05}Ce_{0.95}O₃ compared to un-doped BaCeO₃ nanocatalyst. The 5% Nd-doped nanocatalyst was able to convert almost the totality of CH₄ into CO₂ with only about 8 minutes of reaction. The catalyst lifetime was also improved from 19 min (for un-doped catalyst) to 25 min. However, when the doping level exceeds 5% Nd, the conversion efficiency of CH₄ into CO₂ significantly decreases, even though the catalyst lifetime is remarkably enhanced, as shown in Table 3. These results indicate that the Nd content greatly affects the catalytic properties of BaNd_xCe_(1-x)O₃ nanocatalyst and can thus be optimized to achieve the desired catalytic properties in terms of conversion efficiency and catalyst lifetime. The enhancement of the catalytic properties of 5% Nd-doped BaCeO₃ nanocatalyst compared to un-doped BaCeO₃ is likely due to higher production of oxygen vacancies when the Ce⁴⁺ sites are substituted by the trivalent Nd³⁺ dopant in the BaCeO₃ perovskite structure, which promotes the oxidation of CH₄ (Cheng *et al.* 2016). However, at doping rate higher than 5% Nd (compared to Ce), the quantity of oxygen vacancies produced by the nanocatalyst would be lower because of a significant partitioning of Nd dopant over both Ba and Ce sites, as already reported in the literature (Wu *et al.* 2005). Such partitioning reduces the concentration of oxygen vacancies, which, in turn, would lower the oxidizing ability of Nd-doped BaCeO₃ nanocatalyst. However, further investigations will be carried out for a deep understanding of the effect of Nd doping rate and the role of oxygen vacancies formation on CH₄ conversion efficiency of Nd-doped BaCeO₃ nanocatalyst.

3.2.2 Optimization of CH₄ conversion temperature

5% Nd-doped Barium cerate BaNd_{0.05}Ce_{0.95}O₃ nanocatalyst, which exhibited the highest CH₄ conversion efficiency was selected in order to optimize the conversion temperature of CH₄. A series of catalytic test was thus carried out at different temperatures in presence of BaNd_{0.05}Ce_{0.95}O₃ nanocatalyst. Fig. 8 shows the light-off curve of this material in comparison with the one obtained with Pd/Al₂O₃ commercial catalyst.

Results show that CH₄ conversion efficiency rapidly increases up to a temperature of about 250 °C where conversion rate is almost total. At higher temperatures, the conversion rate remains stable. Interestingly, more than 80 % CH₄ conversion is achieved at temperature as low as 200 °C, which indicates that Nd-doped BaCeO₃ nanocatalyst needs much lower activation temperature compared to noble metal-based catalysts that generally require temperature higher than 500 °C to be active, as shown by Fig. 8.

4. CONCLUSION

Nd-doped BaCeO₃ nanocatalysts, with different Nd doping rate, have been successfully synthesized using a simple sol-gel method starting from acetate precursors in isopropanol solvent. The as-prepared materials have been fully characterized with different characterization methods which confirmed the formation of highly crystallized nano-sized spherical particles with crystallite diameter of 17-20 nm, depending on Nd doping rate. The catalytic performances of the as-prepared nanocatalysts have also been measured through the catalytic conversion of CH₄ into CO₂ at different temperatures. To the best of our knowledge, this is the first application of such nanomaterials for total catalytic conversion of CH₄ into CO₂. The 5% Nd-doped BaCeO₃ nanocatalyst shows the highest CH₄ conversion rate (98%) and improved catalyst lifetime (25 min.) compared to un-doped BaCeO₃ nanocatalyst (95% and 19 min., respectively). Moreover, the light-off curve of 5% Nd-doped BaCeO₃ nanocatalyst showed that the catalyst has much lower activation temperature compared to noble metal-based Pd/Al₂O₃ catalysts. Finally, these results substantiate the great potential of Nd-doped BaCeO₃ nanocatalyst to be applied as an alternative material to noble metal-based catalyst, for the catalytic oxidation of CH₄ into CO₂. The application of such nanocatalysts for the catalytic conversion of CH₄ into syngas and value-added products will also be explored in the near future.

ACKNOWLEDGMENT

We thank both M. J. L Gonzales (IFREMER, Toulon) for helping us during BET measurements and M. M. ISA (L2MP Toulon) for his participation in the FTIR catalytic measurements.

SUPPLEMENTARY MATERIAL

This section includes the Fig. 2: FTIR spectra of active gas (2500 ppm CH₄ in air) recorded before (a) and after (b) 1 minute passing through the catalyst, S2: DTA and TGA curves of the dried precursor gel corresponding to BaNd_{0.05}Ce_{0.95}O₃ product. S3: EDS spectrum of undoped BaCeO₃ nanocatalyst.

FUNDING

This research received no specific grant from any funding agency in the public, commercial, or not-for-profit sectors.

CONFLICTS OF INTEREST

The authors declare that there is no conflict of interest.

COPYRIGHT

This article is an open access article distributed under the terms and conditions of the Creative Commons Attribution (CC-BY) license (<http://creativecommons.org/licenses/by/4.0/>).



REFERENCES

- Arai, H., Yamada, T., Eguchi, K. and Seiyama, T., Catalytic combustion of methane over various perovskite-type oxides, *Appl. Catal.*, 26, 265–276 (1986).
[https://dx.doi.org/10.1016/S0166-9834\(00\)82556-7](https://dx.doi.org/10.1016/S0166-9834(00)82556-7)
- Bhowmick, S., Basu, J., Xue, Y. and Carter, C. B., Hydrothermal synthesis of nanocrystalline barium cerate using hexamethylenetetramine, *J. Am. Ceram. Soc.*, 93(12), 4041–4046 (2010).
<https://dx.doi.org/10.1111/j.1551-2916.2010.03998.x>
- Boucher, O. and Folberth, G. A., New Directions: Atmospheric methane removal as a way to mitigate climate change?, *Atmos. Environ.*, 44(27), 3343–3345 (2010).
<https://dx.doi.org/10.1016/j.atmosenv.2010.04.032>
- Brunauer, S., Emmett, P. H. and Teller, E., Adsorption of gases in multimolecular layers, *J. Am. Chem. Soc.*, 60(2), 309–319 (1938).
<https://dx.doi.org/10.1021/ja01269a023>
- Cheng, Z., Qin, L., Guo, M., Xu, M., Fan, J. A. and Fan, L.-S., Oxygen vacancy promoted methane partial oxidation over iron oxide oxygen carriers in the chemical looping process, *Phys. Chem. Chem. Phys.*, 18(47), 32418–32428 (2016).
<https://dx.doi.org/10.1039/C6CP06264D>

- Cui, X., Li, H., Wang, Y., Hu, Y., Hua, L., Li, H., Han, X., Liu, Q., Yang, F., He, L., Chen, X., Li, Q., Xiao, J., Deng, D. and Bao, X., Room-temperature methane conversion by graphene-confined single iron atoms, *Chem.*, 4(8), 1902–1910 (2018).
<https://dx.doi.org/10.1016/j.chempr.2018.05.006>
- de_Richter, R., Ming, T., Davies, P., Liu, W. and Caillol, S., Removal of non-CO₂ greenhouse gases by large-scale atmospheric solar photocatalysis, *Prog. Energy Combust. Sci.*, 60, 68–96 (2017).
<https://dx.doi.org/10.1016/j.peccs.2017.01.001>
- Friedlingstein, P., O’Sullivan, M., Jones, M. W., Andrew, R. M., Hauck, J., Olsen, A., Peters, G. P., Peters, W., Pongratz, J., Sitch, S., Le Quéré, C., Canadell, J. G., Ciais, P., Jackson, R. B., Alin, S., Aragão, L. E. O. C., Arneeth, A., Arora, V., Bates, N. R., Becker, M., Benoit-Cattin, A., Bittig, H. C., Bopp, L., Bultan, S., Chandra, N., Chevallier, F., Chini, L. P., Evans, W., Florentie, L., Forster, P. M., Gasser, T., Gehlen, M., Gilfillan, D., Gkritzalis, T., Gregor, L., Gruber, N., Harris, I., Hartung, K., Haverd, V., Houghton, R. A., Ilyina, T., Jain, A. K., Joetzjer, E., Kadono, K., Kato, E., Kitidis, V., Korsbakken, J. I., Landschützer, P., Lefèvre, N., Lenton, A., Lienert, S., Liu, Z., Lombardozi, D., Marland, G., Metzl, N., Munro, D. R., Nabel, J. E. M. S., Nakaoka, S.-I., Niwa, Y., O’Brien, K., Ono, T., Palmer, P. I., Pierrot, D., Poulter, B., Resplandy, L., Robertson, E., Rödenbeck, C., Schwinger, J., Séférian, R., Skjelvan, I., Smith, A. J. P., Sutton, A. J., Tanhua, T., Tans, P. P., Tian, H., Tilbrook, B., van der Werf, G., Vuichard, N., Walker, A. P., Wanninkhof, R., Watson, A. J., Willis, D., Wiltshire, A. J., Yuan, W., Yue, X. and Zaehle, S., Global carbon budget 2020, *Earth Syst. Sci. Data.*, 12(4), 3269–3340 (2020).
<https://dx.doi.org/10.5194/essd-12-3269-2020>
- Igenegbai, V. O., Meyer, R. J. and Linic, S., In search of membrane-catalyst materials for oxidative coupling of methane: Performance and phase stability studies of gadolinium-doped barium cerate and the impact of Zr doping, *Appl. Catal. B Environ.*, 230, 29–35 (2018).
<https://dx.doi.org/10.1016/j.apcatb.2018.02.040>
- Jackson, R. B., Solomon, E. I., Canadell, J. G., Cargnello, M. and Field, C. B., Methane removal and atmospheric restoration, *Nat. Sustain.*, 2(6), 436–438 (2019).
<https://dx.doi.org/10.1038/s41893-019-0299-x>
- Lee, J. H. and Trimm, D. L., Catalytic combustion of methane, *Fuel Process. Technol.*, 42(2–3), 339–359 (1995).
[https://dx.doi.org/10.1016/0378-3820\(94\)00091-7](https://dx.doi.org/10.1016/0378-3820(94)00091-7)
- Madhuri Sailaja, J., Vijaya Babu, K., Murali, N. and Veeraiah, V., Effect of strontium on Nd doped Ba_{1-x}Sr_xCe_{0.65}Zr_{0.25}Nd_{0.1}O_{3-δ} proton conductor as an electrolyte for solid oxide fuel cells, *J. Adv. Res.*, 8(3), 169–181 (2017).
<https://dx.doi.org/10.1016/j.jare.2016.12.006>
- Matthews, H. D. and Caldeira, K., Stabilizing climate requires near-zero emissions, *Geophys. Res. Lett.*, 35(4), L04705 (2008).
<https://dx.doi.org/10.1029/2007GL032388>
- Rishee Kumar Singh, Vikas Srivastava, Atul, Ashhad Imam, Mehta, An endeavour to decrease CO₂ outflow through efficient use of supplementary cementitious materials in construction, *J. Environ. Nanotechnol.*, 9(3), 30–33 (2020).
<https://dx.doi.org/10.13074/jent.2020.09.203420>
- Roissnel, T. and Rodriguez-Carvajal, WinPLOTR: A Windows tool for powder diffraction patterns analysis, *Mater. Sci. Forum.*, (378-381), 118–123 (2001).
<https://dx.doi.org/10.4028/www.scientific.net/MSF.378-381.118>
- Senthil Kumar, A., Balaji, R., Puviarasu, P. and Jayakumar, S., Structural and morphological analysis of barium cerate electrolyte for SOFC application, *Mater. Sci.*, 35(1), 120–125 (2017).
<https://dx.doi.org/10.1515/msp-2017-0021>
- Shimazaki, Y., Arai, N., Dunn, T. J., Yajima, T., Tani, F., Ramogida, C. F. and Storr, T., Influence of the chelate effect on the electronic structure of one-electron oxidized group 10 metal(ii)-(disalicylidene)diamine complexes, *Dalt. Trans.*, 40(11), 2469–2479 (2011).
<https://dx.doi.org/10.1039/c0dt01574a>
- Su, X., Yan, Q., Ma, X., Zhang, W., Ge, C., Effect of co-dopant addition on the properties of yttrium and neodymium doped barium cerate electrolyte, *Solid State Ionics.*, 177(11–12), 1041–1045 (2006).
<https://dx.doi.org/10.1016/j.ssi.2006.02.047>
- Wu, J., Davies, R. A., Islam, M. S. and Haile, S. M., Atomistic study of doped BaCeO₃: Dopant site-selectivity and cation nonstoichiometry, *Chem. Mater.*, 17(4), 846–851 (2005).
<https://dx.doi.org/10.1021/cm048763z>
- Yamanaka, S., Fujikane, M., Hamaguchi, T., Muta, H., Oyama, T., Matsuda, T., Kobayashi, S. and Kurosaki, K., Thermophysical properties of BaZrO₃ and BaCeO₃, *J. Alloys Compd.*, 359(1–2), 109–113 (2003).
[https://dx.doi.org/10.1016/S0925-8388\(03\)00214-7](https://dx.doi.org/10.1016/S0925-8388(03)00214-7)